



Thermal characterizations of a large-format lithium ion cell focused on high current discharges



C. Veth ^{a,*}, D. Dragicevic ^a, C. Merten ^b

^a Dt. ACCUotive GmbH & Co KG., Kirchheim unter Teck, Germany

^b Institut für Chemische Verfahrenstechnik, Universität Stuttgart, Germany

HIGHLIGHTS

- Thermal imaging of a large-format lithium ion cell up to 300 A discharge current.
- Long-time stable contact resistance to investigate inner cell characteristics.
- Study on absolute temperature and 3D distribution for cell and battery tests.
- Reveals interdependence between distribution of temperature and local SOC, I, SOH.
- Study of temperature characteristics for miscellaneously aged cells.

ARTICLE INFO

Article history:

Received 17 February 2014

Received in revised form

9 May 2014

Accepted 27 May 2014

Available online 9 June 2014

Keywords:

Lithium-ion

Thermal characteristic

Large-format

High current

Graphite-NMC chemistry

Temperature gradients

ABSTRACT

The thermal behavior of a large-format lithium ion cell has been investigated during measurements on cell and battery level. High current discharges up to 300 A are the main topic of this study. This paper demonstrates that the temperature response to high current loads provides the possibility to investigate internal cell parameters and their inhomogeneity. In order to identify thermal response caused by internal cell processes, the heat input due to contact resistances has been minimized. The differences between the thermal footprint of a cell during cell and battery measurements are being addressed. The study presented here focuses on the investigation of thermal hot and cold spots as well as temperature gradients in a 50 Ah pouch cell. Furthermore, it is demonstrated that the difference between charge and discharge can have significant influence on the thermal behavior of lithium ion cells. Moreover, the miscellaneous thermal characteristics of differently aged lithium ion cells highlight the possibility of an ex-situ non-destructive post-mortem-analysis, providing the possibility of a qualitative and quantitative characterization of inhomogeneous cell-aging. These investigations also generate excellent data for the validation and parameterization of electro-thermal cell models, predicting the distribution of temperature, current, potential, SOC and SOH inside large-format cells.

© 2014 Elsevier B.V. All rights reserved.

1. Introduction

Thermal management of lithium ion batteries is a key issue in order to meet performance, range and lifetime requirements of automotive application. Especially for large-format lithium ion cells and high constant discharge current, which is requested for full electric vehicles, a proper thermal management can extend lifetime and range significantly. Key research tasks concerning lithium ion technology are directly influence by temperature distribution inside the cell. A case in point is the problem of low temperature

performance and lithium-plating due to the strong temperature dependence of internal kinetics [1]. Furthermore, the operation limit of 55 °C and calendaric as well as cycle life, following Arrhenius law [2,3], are strongly affected by temperature. Thermal gradients, which are expected to negatively affect cell aging, are another temperature related issue.

In order to develop a sufficient thermal management strategy, it is essential to know internal and external cell parameters during high current discharges. Therefore, this study presents a comprehensive experimental investigation of these parameters up to 300 A discharge current. Former studies [4,5] are limited to currents smaller than 100 A. Even for these smaller currents, it can observe a significant heat flux from the cell conductors into the cell stack due to electrical contact resistances. In that case, this heat flux is the

* Corresponding author. Tel.: +49 160 869 2935.

E-mail addresses: christianveth@gmx.de, christian.veth@daimler.com (C. Veth).

dominant heat source on the cell surface, masking the heat generation inside the cell originating from internal electrochemical processes. Hence, a solution minimizing the external contact resistance is demonstrated in this paper.

Furthermore, it is important to know the cold and hot spots inside the cell during all operating states for online diagnostic analysis during battery operation. Consequently, this work is also dedicated to the identification of hot and cold spots during different operating states by analyzing measurements on cell and battery level, pointing out the difference between these two test environments as well as their transferability.

The underlying study exhibits results for one lithium ion cell type, providing an experimental standard in order to compare the thermal as well as electrical behavior of lithium ion cells also with different chemistry.

For a thermal management strategy it is not sufficient to know the current cell parameters. In addition to that, models and algorithms are needed to predict the thermal behavior. This kind of models are also necessary in order to support diagnostics, because in common battery designs possibilities and locations for measuring are strongly restricted by limited construction space, cost and cell specifications. The measurements shown here provide excellent data for parametrization and validation of such models. Moreover, electro-thermal models reduce development time and costs significantly during the engineering process by providing the possibility to reduce testing cases and time between iteration steps of potential thermal management strategies.

2. Design of experiment

In order to identify internal cell processes during high current tests, it is necessary to consider special issues in the design of experiment. Furthermore, measuring cell behavior and temperature distribution over the cell in a closed battery system yields to challenges on measurement techniques and systems. These difficulties and the comparability of measurements on cell and battery level will be addressed by presenting the developed design of experiment in the following section.

2.1. Experimental setup on cell level

The investigated lithium ion cell is a 50 Ah pouch cell with graphite anode coated on a copper foil and NMC chemistry on an alumina cathode. The cell contains a highly porous ceramic separator. The dimensions of the cell are around 31 cm in length, 17 cm in height and 1.3 cm in width. The cell exhibits two about 10 cm long tabs on the longitudinal edge.

An overview of the experimental setup on cell level is shown in Fig. 1. The cell is located in a climate chamber on an isolating plastic mat. Thermal imaging measurements are performed to investigate the temperature distribution on the pouch foil of the cell. In order to avoid reflection in the infrared spectra and to ensure a constant emission coefficient on surface the cell was painted in black with a camera lacquer. In addition, all metal surfaces are covered by paper towel. PT-100 electrical sensors are located on the backside of the cell in order to compare the front and backside of the cell faced different boundary conditions. Due to that fact, the temperature profile in the direction perpendicular to the cell stack can be evaluated. Both measurement systems exhibit an accuracy of ± 0.01 K. The camera records with a resolution of 640 times 480 pixels.

The principal task is to develop a long time-stable contact resistance for the connection of the load cables. A comparable small electrical contact resistance is inevitable to study internal cell processes during high current discharges, suppressing the

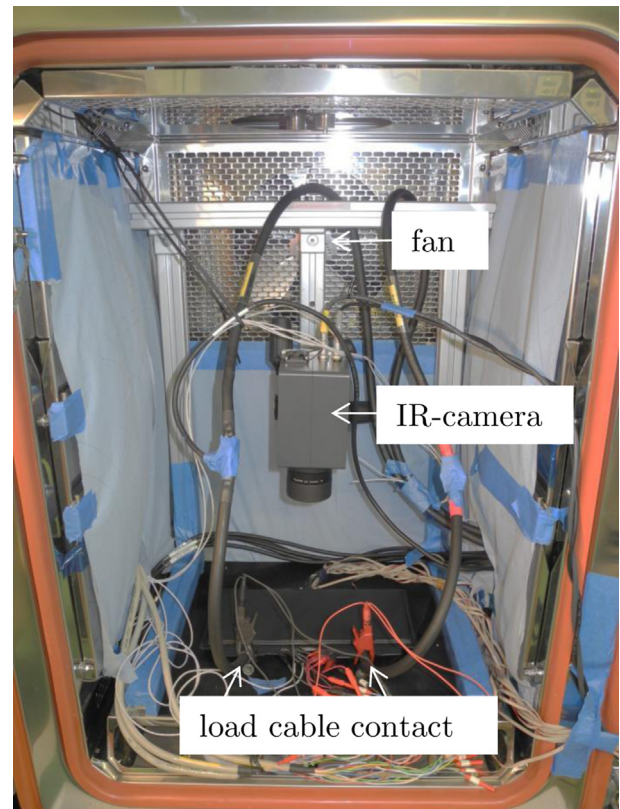


Fig. 1. Experimental setup to perform thermal imaging measurements on cell level; showing lithium ion cell in climate chamber prepared with Tetanal camera lacquer in order to avoid reflections.

dominant heat flow from the contact area inside the cell. To solve this problem it has to be avoided the growth of the oxide layer on the alumina cathode, leading to a high electrical transient resistance. The tests, this study is based on, last for more than one week. In order to ensure comparable and reproducible conditions a bolted connection can not be used. Fig. 2 presents an investigation on the electrical contact resistance for different load cable connections.

The objective is to achieve a long-time stable connection with a contact resistance around $30 \mu\Omega$, which is comparable to a welding used in common batteries. This kind of contact resistance avoids significant heat input into the cell. For instance, a contact resistance of $100 \mu\Omega$ results in a power loss of 9 W during a 300 A discharge, which is almost 10% of the power loss of the full cell. This power dissipates at the small-sized contact area and, therefore, generates a significant heat flow inwards the cell.

Fig. 2 indicates that the untreated bolted connection at the cathode shows a significant increase in contact resistance within a few days in comparison to the untreated anode. Preventing the growth of the oxide layer on the aluminum contact, the cathode contacts isolated from air exhibit also a substantially lower increase for the contact resistance. The best results are obtained with the direct contact of the load cables to the cell conductor preparing the contact surfaces at the cathode with a conductive epoxy containing silver. The nickel coated copper conductor on the anode side exhibits no changes in the contact resistance.

Concerning the comparability between measurements on cell and battery level it has to be mentioned that the connection of the load cables causes non negligible heat extraction from the cell. This can not be prevented without greater effort. Additionally, environmental boundary conditions are different in a battery setup

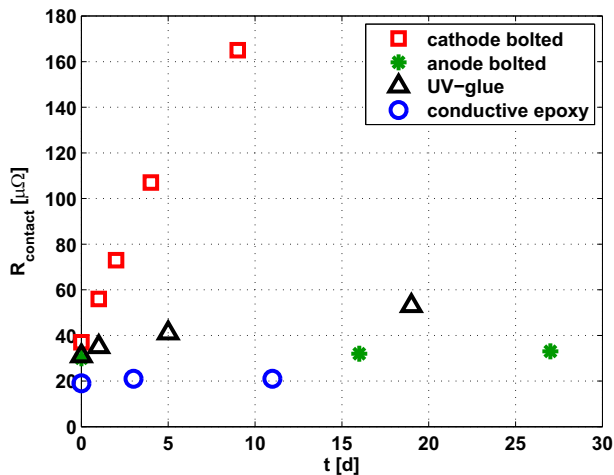


Fig. 2. Electrical contact resistance for different connection types over time after contacting cell conductors with load cables; storage at 25 °C; plotting no preparation with blank cable shoe bolted on cell conductor for anode and cathode, direct connection of the load cable to the cell conductors preparing contact area with UV-glue and contact-60 (anti-corrosion spray) as well as using conductive epoxy in order to avoid growth of oxide layer on cathode.

concerning the surface used for the thermal imaging, which could be avoided with an infrared transmitting thermal isolation.

2.2. Experimental setup on battery level

Temperature measurement inside a battery pack is strongly limited by the construction and installation space. In this battery pack there are two possibilities implemented in order to measure temperature and 3D temperature distribution, presented in Fig. 3.

PT-100 electrical sensors, Fig. 3(a), are used in order to measure temperature on the pouch foil of several cells allocated in the battery pack. Due to the fact that there is enough space between the cells in the stack, it is possible to use these sensors for temperature measurement. In many other battery designs that amount of space is strongly limited. Furthermore, each sensor is connected with four wires to the measurement equipment outside the battery. This is inconvenient and influences heat extraction to the environment. In addition, to identify hot spots inside the battery for different states of operation a large amount of sensors is inevitable. Therefore, a new technique for measuring temperature inside a battery is introduced here. It is based on a fiber optical technique, mainly used for other applications like temperature and strain measurement in tunnels.

This technique uses the Rayleigh back-scatter effect in optical fibers in order to measure temperature [6–8]. The method provides

the possibility to measure the temperature of the optical fiber on a length of 50 m with a resolution of 5 mm and an accuracy of ± 0.1 K. In order to measure temperature on a surface the fiber has to be directly attached to that surface without stressing the fiber, because mechanical stress yields to equivalent signal like a temperature change using this technology. Therefore, the optical fiber is guided in a Teflon tube, which is glued with an UV-adhesive directly to the pouch cell, demonstrated in Fig. 3(b). With that method, the fiber can be guided along the cell surface with minimized friction and mechanical stress. In addition, it has a thermal link to the cell surface in order to measure the cell surface temperature. With the optical fiber technique temperature can be measured at around 10^4 positions in a battery, which exists only one optical fiber with a diameter of around 200 μm .

In conclusion, measuring temperature with an optical fiber provides the possibility to determine the 3D temperature distribution without having measurable influence on the heat transfer to the environment. The accuracy of the system is theoretical in the same range like a PT-100 sensors. Considering the accuracy of the sensor, the position on cell surface and post processing it can be identified a good agreement of the two methods of less than ± 0.2 K.

Battery tests are performed also in the climate chamber in order to adjust miscellaneous, comparable environment conditions. The battery consists of 3 modules. The modules are fixed inside a battery housing. Every module contains 31 cells stacked next to each other. The cells are fixed with plastic cell holders. Cells are directly connected due to the electrical series connection by welding. There is no direct contact between neighbored cell in the stack. The cells are separated by an air gap of a few millimeters. The module is mounted in the housing with alumina end-plates which are isolated from first and last cell stack by isolating tape.

2.3. Test cases

To meet all requirements described in Section 1 several sets of experiments have to be performed. In order to investigate the temperature performance of the cell at miscellaneous currents and ambient temperatures, constant current discharges were performed in the range of 300 A to 12 A as well as constant current charges from 100 A to 12 A. On battery level the maximum current is limited to 150 A, because of upper temperature limit. During some charges also a constant voltage phase were done, subsequently the constant current phase, to address the 100% state of charge (SOC). In order to have a direct comparison between charge and discharge, charges and discharges were performed with identical Ah-throughput in the same SOC region. These tests were carried out at three different ambient temperatures 25 °C, 0 °C and –20 °C. Relaxation breaks to ambient temperature have been made between the load cases. While the relaxation phases also the

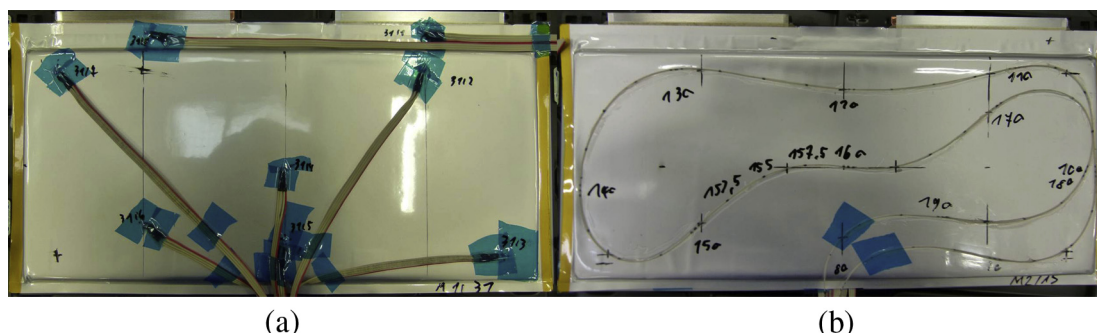


Fig. 3. (a) PT-100 Sensor on cell; (b) optical fiber in Teflon tube glued on cell.

internal electrical and chemical parameters of the cell become homogenous. These tests were performed identically on cell and battery level. A case in point is Fig. 4 illustrating a current profile over time at 25 °C.

For model validation and parametrization, it is also necessary to perform tests which can be used in order to separate the influence of the boundary conditions from electrical cell performance. Therefore, cooling and heating curves were measured by changing environment temperature without current load. Additionally, on battery level characteristic curves were measured changing cooling inlet temperature and mass flow through the battery without electrical load and with electrical load. Furthermore, in order to address various electrical dynamics during validation tests with synthetic and real driving cycles were performed.

3. Study of high current discharges of large-format lithium ion cells

In this section the results of the measurements on cell and battery level will be discussed, focusing on temperature gradients, distribution as well as absolute temperature. Furthermore, the possibility will be demonstrated to investigate internal cell parameters with spatially resolved temperature measurements at the cell surface. The analysis is based on the various constant current discharges (DCH) and charges (CH) at miscellaneous ambient temperatures.

3.1. Temperature distribution and gradients on cell level

Hot spots, cold spots, temperature distribution and gradients can be investigated properly with the thermal imaging technique. Fig. 5 presents the temperature development during a 300 A DCH.

At the start of the DCH, the dominant effect on temperature distribution is the local power loss and, therefore, the current distribution in the cell. This can be deduced from the hot spot of the cell at the terminals, see Fig. 5(a) and (b). Current distribution in a homogenous cell is only determined by the electrical resistance of the metal conductor foils and the position of the current collectors. Due to the conductor geometry, the test exhibits hot spots near the terminals and slightly higher temperatures at the negative side. The higher current density near the negative terminal results from the higher electrical resistance of the copper foil in comparison to the aluminum foil inside this cell, which is two times thicker than the

copper foil. Since, the copper foils of the anodes are connect to the negative terminal, the current density there is slightly higher, resulting in a higher power loss there. This is equivalent for CH.

In case of inhomogeneous cell parameters due to geometrical asymmetries, as mentioned, or due to boundary conditions, internal processes can enforce or damp the external driven gradient. Neglecting the electrical resistance of the thin conductor foils, the cell can be considered as an electrical parallel circuit of small elementary cells, since the metal foil resistances are much lower than the local resistance of the elementary cell. The resistances of the metal foils are in the order of magnitude of 10 $\mu\Omega$ and the local resistance of the elementary cell is significant higher than the full cell resistance, which is the order of 1000 $\mu\Omega$. In an electrical parallel circuit the power loss scales U^2/R . Therefore, regions of lower electrical resistance dissipate more power than regions with higher electric resistance due to the smaller current density in regions with higher resistance. This is the dominating effect even for small temperature or SOC gradients. For instance a temperature variation of 5 K at 25 °C and 50% SOC results in a change of 100 $\mu\Omega$ in cell resistance. These changes increase dramatically for low SOC's and temperatures.

The internal cell resistance decreases with temperature and SOC [9]. Due to the fact that more heat is dissipated in hotter areas of the cell than in colder areas, the electric system itself is inherently unstable concerning temperature gradients. It is stabilized due to heat conductance and SOC differences. This is confirmed by Fig. 5(b) indicating that the hot spot of the cell shifts consequently to the negative terminal till the middle of the DCH. This is also confirmed by steadily increasing temperature differences on the cell surface during the DCH, presented in Fig. 7.

Increasing difference between ambient and cell temperature results in a migration of the hot spot towards the center of the cell, because of increasing impact of the environmental boundary conditions i.a. heat extraction due to the load wires at the tabs. The hot spot at the end of the discharge, presented in Fig. 5(c), is a superposition of the hot spot induced by the boundary conditions and the hot spot induced by the internal cell parameters and geometry. The effect of the boundary conditions, depending on ambient temperature, can also be investigated from Fig. 6 presenting thermal images during a 300 A DCH with different ambient temperatures.

At lower temperatures the external heat extraction becomes more dominant due to higher the temperature difference between cell and environment, resulting in a hot spot farther located from the terminals for the DCH at lower ambient temperature. The shift of the hot spot to the negative terminal, due to the electrical cell design, can also be observed for lower ambient temperature. A total change of the hot spot position can be observed studying DCHs at various ambient temperatures for aged cells. The hot spot position for aged cells exhibits increased temperature dependence due to the temperature dependent gradient of the local cell resistance, which develops during inhomogeneous degradation. This effect can be observed during measurements with the aged cells introduced in Section 3.5.

Fig. 7 presents the temperature difference on cell surface and its development over time for various currents and ambient temperatures. It can be observed that the temperature difference on cell surface increases with current and decreases with ambient temperature. Consequently, the gradient increases throughout with higher dissipated heat. This confirms the statement, that the electrical system of the cell is inherently unstable concerning temperature differences. As it is mentioned previously, in hotter areas more heat is dissipated than in colder areas. The gradient increases continuously during a complete DCH, which also means that the stabilization due to SOC gradients and heat conductivity is not

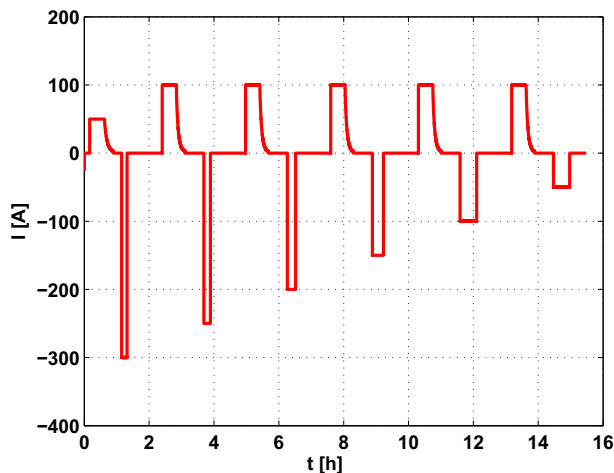


Fig. 4. Example of current profile over time at 25 °C for test on cell level in climate chamber; discharge current is illustrated with negative values.

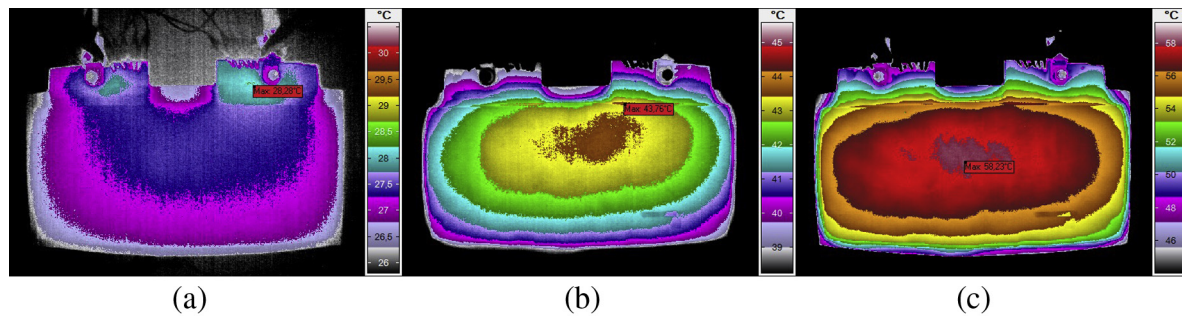


Fig. 5. Comparison of thermal images at different time points during a 300 A discharge with ambient temperature 25 °C equivalent to the starting temperature; showing thermal images at (a) begin of discharge (10 s); (b) middle of discharge (maximum temperature is half of temperature at the end of the discharge; 250 s); (c) end of discharge (585 s); negative terminal on the right hand side and positive terminal on the left; maximum temperature at the left upper corner of the red text box. (For interpretation of the references to color in this figure legend, the reader is referred to the web version of this article.)

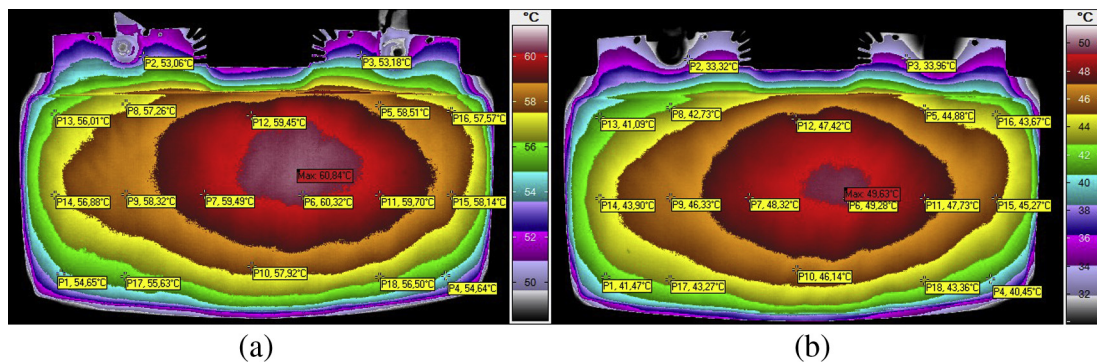


Fig. 6. Comparison of temperature distribution at the end of a 300 A DCH with ambient temperature (a) 25 °C and (b) 0 °C; showing absolute values for specific points.

dominant yet. Due to the change of the hot spot position, resulting in the change of the region with minimum SOC, the cell does not reach low SOC's smaller than 2% in any region of the cell. SOC's lower than 2% result in a significant increase of the cell resistance in the hottest area, which is also the area with lowest SOC. This effect results in decreasing temperature gradient. That is described more in detail in the following subsections.

3.2. Dependence of absolute temperature on current and ambient temperature

It is mentioned previously that the temperature increase at the end of a DCH decreases with ambient temperature and increases with DCH current. Fig. 8 indicates the dependence of the maximum temperature increase at the end of the DCH on DCH current and ambient temperature.

Fig. 8(a) demonstrates that the maximum temperature increase of the cell at the end of the DCH depends linearly on the DCH current. The slope decreases with ambient temperature. Only for low temperatures and very low DCH current, the heat losses to the environment become dominant and it is observed a slight deviation from this linear trend. The linear relation results from the compensation of two effects. Higher current results in higher power loss, exhibiting a quadratic dependence. This leads to higher temperatures which implies lower internal cell resistance, decreasing exponentially with temperature. Additionally, an indirect proportional relation is identified between the starting temperature and the maximum temperature increase of the cell at the end of the DCH, demonstrated by Fig. 8(b). This relation originates similarly from the compensation of two effects. The lower temperature results in higher cell resistance, already mentioned, but

the higher cell resistance implies additionally a significant smaller Ah-performance of the cell while constant current DCHs.

These results are dominated by the internal processes of the cell and depend marginal on the boundary conditions, since these dependencies can also be identified in battery measurements with totally different boundary conditions. The single difference between cell and battery measurements is the absolute temperature

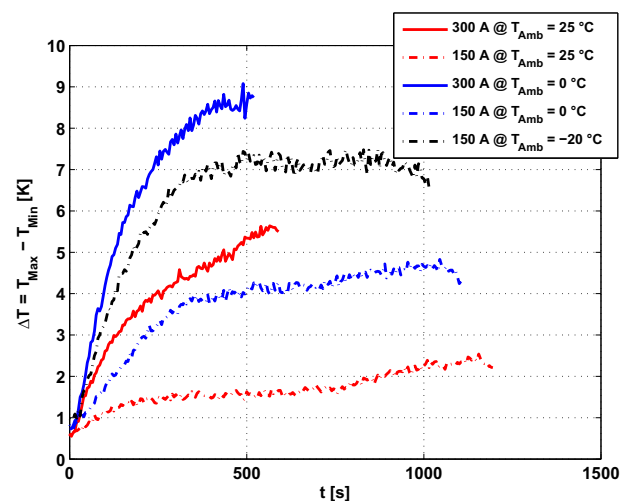


Fig. 7. Time development of the temperature difference over cell for different DCH currents and starting temperatures; showing difference between minimum and maximum temperature of 24 equal distributed positions on cell surface; constant current DCHs from 100% SOC to 3 V cell voltage.

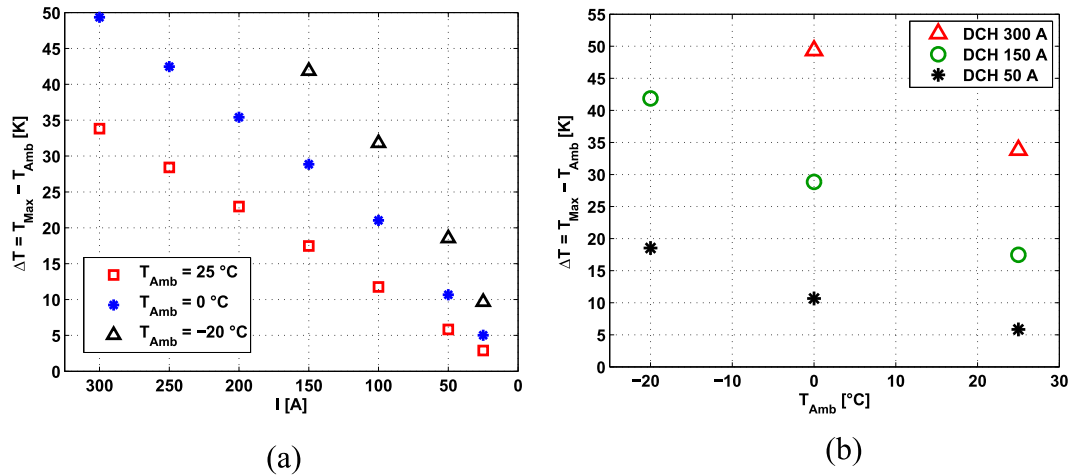


Fig. 8. Dependence of the temperature increase during a full DCH (difference between starting cell temperature (equal ambient temperature) and temperature at the end of the DCH) on (a) DCH current; (b) ambient temperature; showing linear relationship for both dependencies.

influenced by the boundary conditions, however the dependencies are equivalent. In addition, tests with three different cells of this type exhibit a maximum difference in the temperature increase at the end of the discharge lower than 3%.

These proportionalities provide the possibility of a direct temperature prediction on the battery management system. During operation, knowing these dependencies, the maximum temperature increase at the end of a full DCH cycle can be predicted from the diagnostic of present temperature and mean current. Thermal management can be improved by starting, stopping or controlling cooling depending on maximum possible temperature of the cells at the end of the cycle in order to reach range and lifetime requirements. This will provide the possibility for downsizing cooling and securing over temperatures.

3.3. Temperature distribution and gradients on battery level as well as comparison with cell level

In this section the results of the measurements on battery level, specified in Section 2.2, are presented and compared with the

results on cell level. Fig. 9(a) presents the temperature differences over a cell located in the center of a module with 31 cells.

The gradient over cell on battery level exhibits identical dependencies like the gradient during measurements on cell level. The gradient increases with current and decreases with ambient temperature. Furthermore, the temperature difference over the module, illustrated in Fig. 9(b), increases with current and decreases with ambient temperature. In general, the gradient over the module is smaller at the beginning of the DCH and starts to dominate from middle of the DCH. At the end of the DCH the gradient over module is around two times higher than the gradient on cell level.

Fig. 9(a) demonstrates that during some full DCHs the gradient over cell on battery level does not increase continuously. The point in time, after which the temperature difference starts to decrease, depends on the height of the gradient. One reason could be the heat extraction from the cell stabilizing the gradient based on the cell geometry. However, the heat extraction to the environment is significantly lower for battery tests in comparison to cell level tests, which do not exhibit this phenomenon. The other reason is that

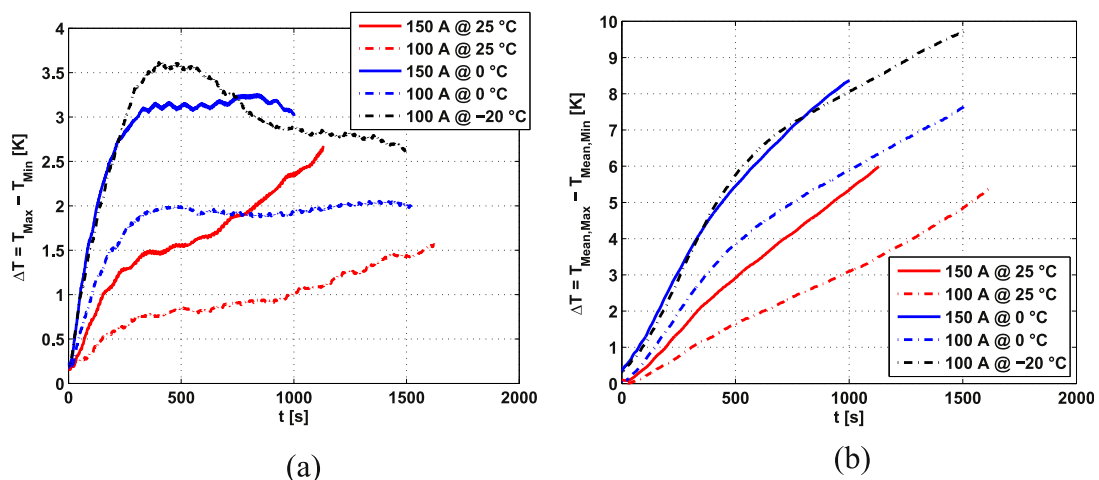


Fig. 9. Temperature differences on battery level for different ambient temperatures and currents, resulting from full constant current DCHs: (a) temperature difference over cell located in the center of a module with 31 cells, presenting temperature difference of minimum and maximum temperature of six sensors asymmetric distributed over cell surface; cell with medium voltage level in comparison to all cells; (b) temperature difference over module considering mean cell temperatures, showing difference between maximum and minimum of cell mean temperatures in one module.

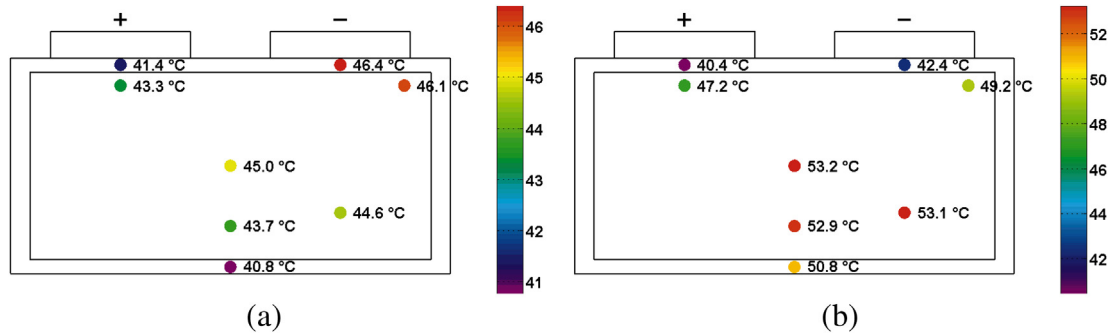


Fig. 10. Temperature distribution over cell on battery level at the end of a 150 A DCH: (a) no active water cooling and $T_{amb} = 25^\circ\text{C}$; (b) with conductor tab cooling and $T_{amb} = 45^\circ\text{C}$.

without dominant heat losses to the environment, the hot spot in the cell does not move during a full DCH. Thus, the current distribution is stable for most of the DCHs, resulting in a steadily increasing SOC gradient with lowest SOC at cell hot spot. In case, the SOC becomes lower than 2% the internal resistance of this cell region starts to increase dramatically resulting in decreasing power loss in this area. Therefore, the temperature in hotter areas increases slower and current density increases in the colder areas, which results in the decrease of the temperature difference over the cell.

Fig. 10(a) illustrates the temperature distribution of a cell at the edge of the module during a DCH without cooling. The hot spot is located on the top of the cell shifted to the negative terminal, which has the same position as at the beginning of a DCH on cell level, presented in Fig. 5(a) and (b). The hot spot does not move during battery tests because of non dominant heat extraction. In comparison to that, during tests on cell level the hot spot migrates because of the heat extraction due to load wires as well as forced convection.

In case of tab cooling the cell hot spot at the end of a full DCH is in the center of the lower half of the cell, illustrated in Fig. 10(b).

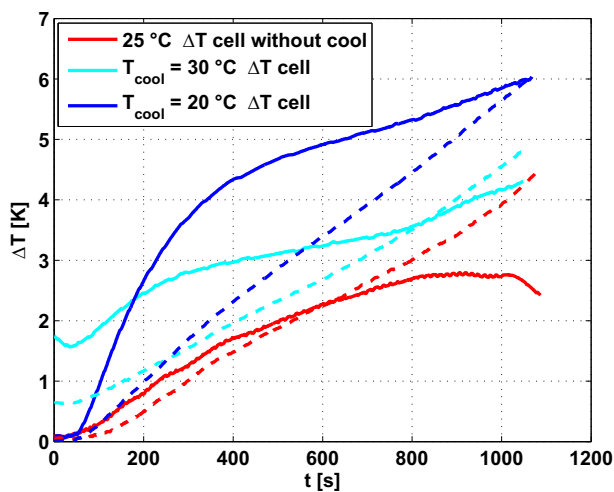


Fig. 11. Comparison of temperature difference over module and cell between no active water cooling and with conductor cooling, considering two different cooling inlet temperatures; tests were done with 150 A DCH current; full lines are differences between maximum and minimum temperature of a specific cell at the edge of a module; dashed lines are differences between maximum and minimum mean cell temperatures over the module; test without active water cooling was done with 25°C ambient temperature tests with active tab cooling were done at $T_{amb} = 45^\circ\text{C}$, resulting in comparable absolute temperatures for tests without and with active water cooling.

During a DCH with active cooling, the hot spot migrates from the position on the tab, which is the same position as in the case of measurements without cooling, to the position in the lower half of the cell till the end of the DCH. Fig. 11 presents the comparison of the temperature difference over cell and over battery pack between DCHs with conductor cooling and without active water cooling. This comparison exhibit that the temperature gradient over the module slightly increases with cooling and that the gradient over the cell strongly increases with decreasing cooling inlet temperature. With active cooling the gradient over the cell becomes the dominant gradient in a battery pack. Consequently, running the cooling system with small difference between cooling inlet and mean cell temperature can decrease the gradient over battery pack, which might slightly increase the temperature difference over some cells.

The difference in temperature over cell does not decrease at the end of the DCH for tests with cooling in comparison to a DCH without active water cooling, which might be due to the smaller SOC difference during a DCH with cooling. Like mentioned above, the hot spot moves from the conductor area to the lower half of the cell stack, due to the heat extraction at the tabs. This results in lower SOC differences at the end of the DCH. Hence, the hottest region in the cell at the end of the DCH with cooling does not reach very low SOC, which would induce significant increase of local cell resistance, before the DCH is stopped due to the 3 V voltage limit of the cell. This is equivalent to the observation presented for measurements on cell level due to the heat extraction by environmental boundary conditions.

Hot spot migration during DCH and different hot spot position, which depends on the operating condition of the battery, result in difficulties concerning temperature diagnostics in vehicle application. Because of strongly limited space and cost for this application, the possible number and positions of temperature sensors in a battery produced in series are rare. Hence, there is a need on diagnostic analysis with temperature algorithms and three dimensional temperature models in order to meet the demands described in Section 1 like battery lifetime.

In Fig. 12 comparison between battery and cell level is presented, considering the absolute temperature and temperature difference over cell surface. The absolute temperature on battery level shows a significant sharper increase, illustrated in Fig. 12(a). The maximum temperature difference at the end of the DCH on battery level is about 10 K higher than on cell level. The shape of the curves for cell and battery level is similar. Hence, it is dominated by internal cell processes. The relaxation times are also significantly higher for battery level due to the lower heat losses to the environment.

Fig. 12(b) indicates comparable temperature differences over the cell for measurements on battery as well as cell level,

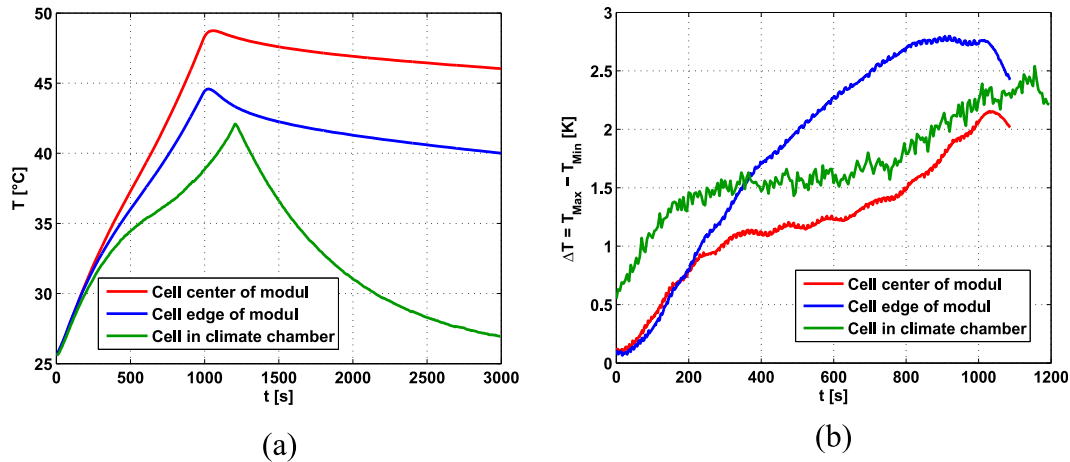


Fig. 12. Comparison between measurements on cell and battery level: (a) absolute mean temperature; (b) difference in temperature over cell; showing 150 A DCH with $T_{\text{amb}} = 25^\circ\text{C}$; considering measurement data from thermal imaging for cell level and temperature measurement for cell in the center of module and cell at the edge of a module; cell in center of module has higher voltage level than cell at the edge of the module.

considering cells with identical voltage levels. This is the case for the cell in the center of the module and the cell tested in climate chamber. Thus, the temperature gradient over the cell is primarily due to internal heat dissipation mechanism and not significantly influenced by boundary conditions like heat losses to the environment. This figure also indicates the decreasing temperature difference at the end of the DCH for the cell at the edge of the module. This cell has lower voltage and SOC level at the end of the DCH in comparison to the cell in the center of the module.

3.4. Differences between charge and discharge due to entropy effects

In this section a study on differences between CH and DCH is presented. Most of lithium ion cells exhibit different thermal response during DCH and CH. In literature contradictory statements concerning the entropy effect in lithium ion cells can be found. Reversible heat generation induces miscellaneous temperature development during CH and DCH. For instance in some textbooks like [10] it is stated that the reversible heat effect, due to entropy, can be neglected for lithium ion cells. Several hints that the entropy

effect has significant influence on the thermal behavior of lithium ion cells can be deduced from Refs. [11,12].

Fig. 13 illustrates the difference between CH and DCH with a current of 25 A. These graphs exhibit a significant difference between CH and DCH. If this difference is only due to reversible heat effects, the derivative of the temperature with respect to the time presented in Fig. 13(b) would be axis-symmetric with regard to a parallel to the x-axis. The cell, under investigation, exhibits slight deviations from that symmetry. Thus, in addition to reversible heat effects the heat dissipation mechanisms during intercalation and deintercalation of lithium might be different. This statement can be proven with an electro-thermal model.

Fig. 13(a) exhibits a cooling effect at the beginning of the CH due to the entropy effect. A cell temperature lower than ambient temperature is measured. Strong entropy effects can be observed for SOC's lower than 30% and greater than 75%, which heat up the cell during DCHs and cool the cell during CHs. This kind of thermal characteristic can be observed also for other cells with NMC chemistry.

The reversible heat effect due to entropy effects can be derived from thermodynamic energy equation,

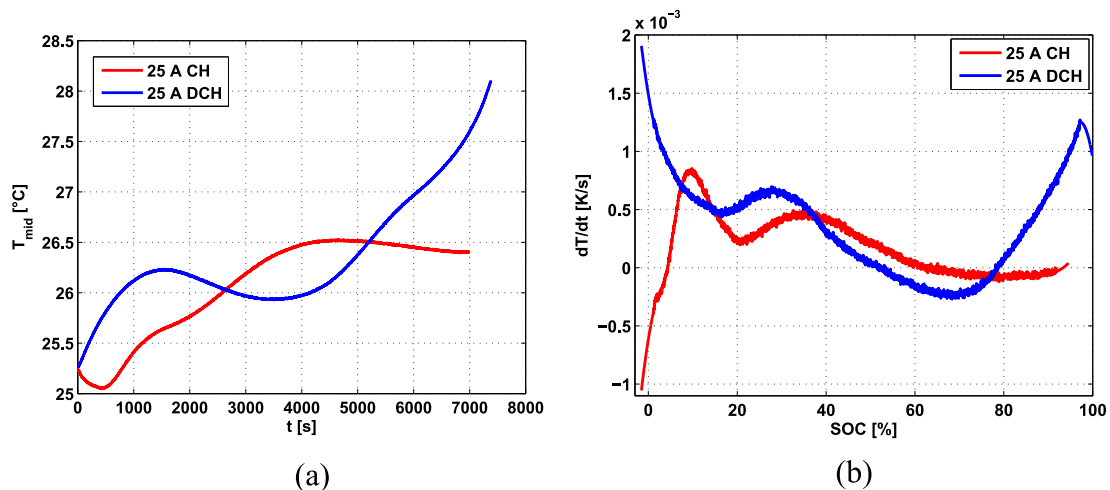


Fig. 13. Differences between 25 A CH and 25 A DCH at $T_{\text{amb}} = 25^\circ\text{C}$; (a) temperature in the middle of the cell over time; (b) derivative of temperature with respect to time over state of charge.

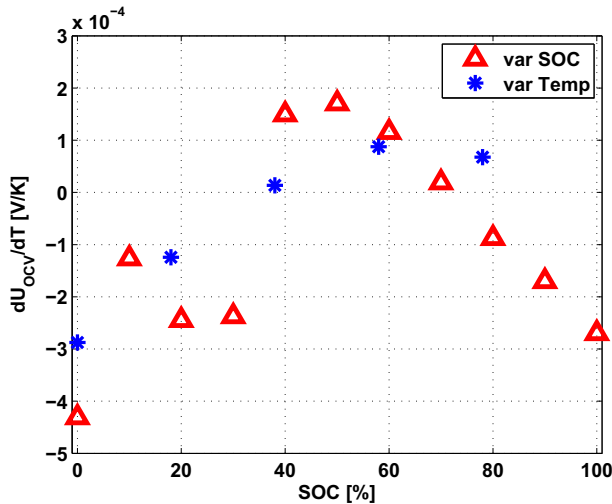


Fig. 14. Derivative of open circuit voltage with respect to temperature over state of charge; red triangles result from measurement by setting different temperature and varying SOC at one given temperature in order to challenge self DCH problems; blue stars result from measurement by setting SOC at $T_{\text{amb}} = 25^\circ\text{C}$ and varying ambient temperature at one given SOC in order to challenge the problem of long relaxation times after a current pulse especially at low temperatures. (For interpretation of the references to color in this figure legend, the reader is referred to the web version of this article.)

$$\Delta H = \Delta G + T\Delta S. \quad (1)$$

So the entropy term derives as [10,13]

$$T\Delta S = T \left(-\frac{d\Delta G}{dT} \right) = T \left(nF \frac{dU_{\text{OCV}}}{dT} \right). \quad (2)$$

Thus, the entropy term can be determined by measuring the dependence of the open circuit potential (U_{OCV}) on cell temperature. These measurements require a very exact voltage measurement (± 1 mV) especially for cells with high capacity, due to the fact that small voltage differences result in a relatively high entropic heat. This is deduced from Eq. (2), in which the voltage derivative with respect to temperature is multiplied by cell capacity. Hence, during these measurements influences on open circuit voltage, for instance due to self discharge, temperature dependent hysteresis etc., have to be prevented.

In order to address self DCH problems, measurements have been done varying the SOC at a given temperature with break times for voltage relaxation. These measurements are time-intensive due to relaxation times of more than eight hours at small temperatures. In order to face the problem of long relaxation times after a current

pulse, additional measurements have been performed in which the SOC is set at 25°C and relaxation is done at high temperatures. After relaxation, ambient temperature is varied, followed by sufficient relaxation times, in order to measure the open circuit voltage for different temperatures.

Fig. 14 presents the results for both types of measuring the derivative of OCV with respect to temperature over SOC. Fig. 14 confirms the observations in Fig. 13. Both demonstrate an entropy effect resulting in significant heating of the cell during DCH and cooling during CH for SOC $\leq 30\%$ and greater than 75% . A value of $-3.5 \cdot 10^{-4} \text{ VK}^{-1}$ results in a reversible power of around $P_{\text{rev}} = T\Delta S/t_{\text{DCH}} \approx 5 \text{ W}$ during a 50 A DCH. This contribution to the heat balance is in the same order of magnitude as the electrical dissipation power which is around 10 W . Therefore, the reversible heat effect can not be neglected in thermal studies and models.

Two sign changes of the entropic power can be observed around 35% – 40% and 75% SOC, which is equivalent to $x = 0.26$ and $x = 0.48$ for Li_xC_6 as well as $y = 0.81$ and $y = 0.61$ for Li_yNMC_2 . These entropy changes are in agreement with that in literature proposed NMC lattice phase transition for SOC $\leq 30\%$ and 75% – 95% SOC [14–16] as well as the entropy changes for disordered carbon and graphite for SOC $\leq 35\%$ [17–19]. These entropy terms measured and presented in Fig. 14 show also total agreement with temperature development illustrated in Fig. 13. Even the small increase of dU_{OCV}/dT around 10% – 15% SOC can also be observed in the small reduction of the temperature increase in Fig. 13 around 6000 s and 10% – 15% SOC, respectively.

The entropy effect exhibits no dependence on temperature which supports the statement of entropy effects due to lattice phase transition and intercalation entropy, depending only on SOC. Thus, the differences between CH and DCH observed in measurement can be mostly explained by reversible heat due to entropy effects.

3.5. Thermal imaging of miscellaneously aged cells

Thermal characterization based on infrared imaging measurement provides also the possibility of a non-destructive post-mortem analysis. Fig. 15 presents thermal images of miscellaneously aged cells at the end of a high current DCH (250 A).

These pictures indicate totally different responses for each cell with different hot and cold spot positions as well as gradients. The gradient over cell increases with higher internal cell resistances and local inhomogeneities of cell resistance and SOH (state of health). Gradients up to 15 K for aged cells can be observed in comparison to 7 K for new cells.

The shift of the hot spots and the increasing gradients over lifetime provide an additional complexity for temperature diagnostics in batteries for vehicle application. The determination of

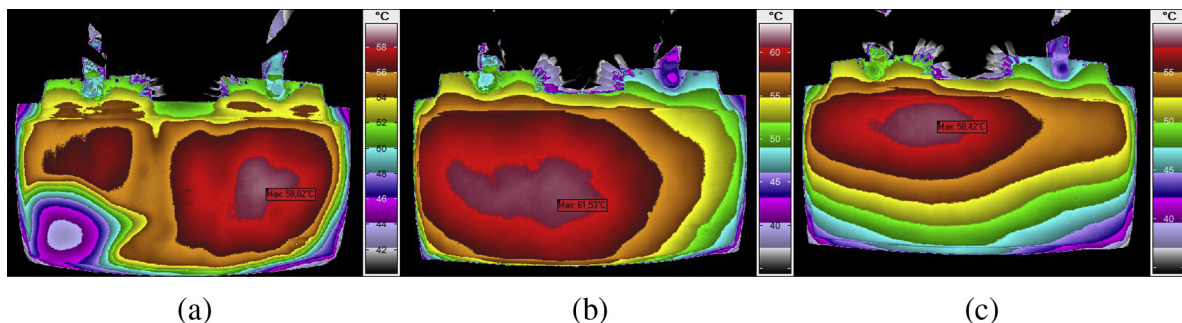


Fig. 15. Thermal images at the end of a 250 A DCH for miscellaneously aged cells at $T_{\text{amb}} = 25^\circ\text{C}$; (a) calendaric aged cell ($C_{\text{rest}} = 87\%$); (b) high current cycled aged cell ($C_{\text{rest}} = 74\%$); (c) low current cycled aged cell ($C_{\text{rest}} = 75\%$); negative terminal at the right hand side and positive terminal on the left.

local temperature inside the cells is not possible with common electrical sensors. A possible method of a sufficient temperature diagnostic over lifetime is proposed in Section 2.2. The prediction of local aging effects, and the resulting temperature response, is not trivial and under development.

Thermal imaging provides the possibility to identify local aging effects as well as electrically inactive areas in aged cells, which exhibit areas with strongly increased internal cell resistance and reduced capacity. Due to the fact that in areas with higher local cell resistance less heat is dissipated, because of the primarily parallel connection of these areas, the distribution of internal parameters like cell resistances can be indirectly determined from the temperature distribution on the cell surface. A case in point is illustrated in Fig. 15(a). The calendaric aged cell exhibits a moving inactive area in the corner of the cell. This can be identified as a gas pocket inside the cell. The gas pocket has negative effect on internal cell resistance and is reversible. The high current cycled cell indicates increased internal cell resistance near the negative terminal, Fig. 15(b). This characteristic can also be identified for the low current cycled cell, Fig. 15(c), which exhibits also an extended inactive area at the lower edge of the cell. This inactive area can be ascribed to lithium plating, resulting additionally in higher cell thickness at the lower edge of the cell.

4. Conclusions and future work

In conclusion, this paper presents a comprehensive 3D thermal characterization of a large-format lithium ion cell up to very high DCH currents. It presents temperature distribution over large-format lithium ion cells and the positions of the hot spot during full DCHs. Furthermore, it is demonstrated that increasing the power of batteries for full electric vehicles will result in difficulties concerning temperature diagnostic due to temperature gradients as well as local hot and cold spots. In particular, it will be challenging to ensure a sufficient diagnostic in order to secure operating windows over lifetime, because of changing thermal characteristics over lifetime. Due to strong limitations on costs and space in vehicle application, it is mandatory to extend temperature diagnostic by thermal models, predicting temperature distribution over cell in real time. Therefore, temperature diagnostic and management will be a key issue in order to meet performance and lifetime demands in future electric vehicles with higher weight.

The underlying work is pointing out the difference in temperature development between cell and battery level. Moreover, the effect of tab cooling on temperature distribution and gradients is presented in this paper. Measurements of the reversible heat effect due to entropy, based on intercalation processes, establish the

statement that reversible heat effects have significant influence on the heat balance of lithium ion cells with graphite-NMC chemistry.

Measuring the temperature distribution on cell surface also provides the possibility of a non-destructive post-mortem analysis for large-format lithium ion cells. Miscellaneously aged cells indicate completely different temperature response and exhibit strong local aging effects, resulting in electrically inactive areas. The paper demonstrates that thermal measurements are predestined to investigate internal parameters like temperature, current, potential, SOC and SOH as well as their distribution and gradients. Since, this study points out the direct correlation between these parameters.

The experimental design proposed in Section 2 and the experimental data additionally provide the possibility to develop and validate electro-thermal models for large-format lithium ion cells up to high currents. The qualitative statements on internal cell parameters and their gradients can be underlined with a quantitative statement using such validated models. This kind of models has been developed applying the data collected in this study and will be presented in further publications.

References

- [1] S. Tippmann, D. Walper, L. Balboa, B. Spier, W.G. Bessler, *J. Power Sources* 252 (2014) 305–316.
- [2] M. Broussely, P. Biensan, F. Bonhomme, P. Blanchard, S. Herreyre, K. Nechev, R. Staniewicz, *J. Power Sources* 146 (1–2) (2005) 90–96.
- [3] K. Asakura, M. Shimomura, T. Shodai, *J. Power Sources* 119–121 (2003) 902–905.
- [4] U. Seong Kim, J. Yi, C.B. Shin, T. Han, S. Park, *J. Electrochem. Soc.* 158 (5) (2011) A611–A618.
- [5] A. Pesaran, The 21st Worldwide Battery, Hybrid and Fuel Cell Electric Vehicle Symposium & Exhibition, Monaco.
- [6] D. Gifford, B. Soller, M.S. Wolfe, M. Froggatt, in: 31st European Conference on Optical Communication (ECOC 2005), vol. 3, 2005, pp. 511–512.
- [7] M. Froggatt, J. Moore, *Appl. Opt.* 37 (10) (1998) 1735–1740.
- [8] B. Lee, *Opt. Fiber Technol.* 9 (2) (2003) 57–79.
- [9] D. Andre, M. Meiler, K. Steiner, C. Wimmer, T. Soczka-Guth, D. Sauer, *J. Power Sources* 196 (12) (2011) 5334–5341.
- [10] A. Jossen, W. Weydanz, *Moderne Akkumulatoren richtig einsetzen*, Ubooks, 2006.
- [11] S.A. Hallaj, J. Prakash, J. Selman, *J. Power Sources* 87 (1–2) (2000) 186–194.
- [12] T.M. Bandhauer, S. Garimella, T.F. Fuller, *J. Electrochem. Soc.* 158 (3) (2011) R1–R25.
- [13] K. Thomas, J. Newman, R. Darling, in: W. Schalkwijk, B. Scrosati (Eds.), *Advances in Lithium-Ion Batteries*, Springer, US, 2002, pp. 345–392.
- [14] K. Takano, Y. Saito, K. Kanari, K. Nozaki, K. Kato, A. Negishi, T. Kato, *J. Appl. Electrochem.* 32 (3) (2002) 251–258.
- [15] K.E. Thomas, J. Newman, *J. Power Sources* 119–121 (2003) 844–849.
- [16] R.E. Williford, V.V. Viswanathan, J.-G. Zhang, *J. Power Sources* 189 (1) (2009) 101–107.
- [17] Y.F. Reynier, R. Yazami, B. Fultz, *J. Electrochem. Soc.* 151 (3) (2004) A422–A426.
- [18] Y. Reynier, R. Yazami, B. Fultz, *J. Power Sources* 119–121 (0) (2003) 850–855.
- [19] V.A. Sethuraman, L.J. Hardwick, V. Srinivasan, R. Kostecki, *J. Power Sources* 195 (11) (2010) 3655–3660.